Non-equivalent Atomic Vibrations at Interfaces in a Piezoelectric Superlattice

Eric R. Hoglund[1,2*‖], Harrison A. Walker[3,4‖], Md. Kamal Hussain[5], De-Liang Bao[3], Haoyang Ni[6,7,1], Abdullah Mamun[4], Jefferey Baxter[1], Asif Khan[4], Sokrates T. Pantelides[3,4,9+], Patrick E. Hopkins[2,8,10°], and Jordan A. Hachtel[1♠]

[1] Center for Nanophase Materials Sciences, Oak Ridge National Laboratory, Oak Ridge, TN 37830, USA
[2] Dept. of Materials Science and Engineering, University of Virginia, Charlottesville, VA 22904, USA
[3] Dept. of Physics and Astronomy, Vanderbilt University, Nashville, TN 37235, USA
[4] Interdisciplinary Materials Science Program, Vanderbilt University, Nashville, TN 37235
[5] Dept. of Electrical Engineering, University of South Carolina, Columbia, SC 29208, USA
[6] Dept. of Materials Science and Engineering, University of Illinois at Urbana-Champaign, Urbana, IL 61820, USA
[7] Materials Research Laboratory, University of Illinois at Urbana-Champaign, Urbana, IL, USA
[8] Dept. of Mechanical and Aerospace Engineering, University of Virginia, Charlottesville, VA 22904, USA
[9] Dept. of Electrical and Computer Engineering, Vanderbilt University, Nashville TN 37235, USA
[10] Dept. of Physics, University of Virginia, Charlottesville, VA 22904, USA

‖Contributed equally to the paper
*erh3cq@virginia.edu
+pantelides@vanderbilt.edu
°peh4v@virginia.edu
♠hachtelja@ornl.gov

Contents

S1 Supplementary Information: Figures

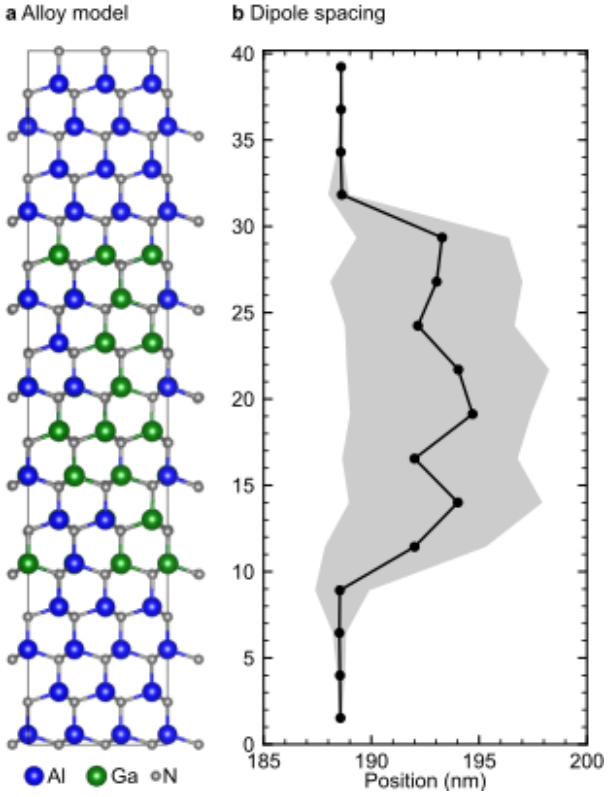

Figure S1. Alloy dipole spacing. (a) Model of an AlN-($Al_{0.65}Ga_{0.35}$)N superlattice along the a-axis. (b) Dipole spacings with the solid black line indicating the average value and the grey span bounding the minimum and maximum values.

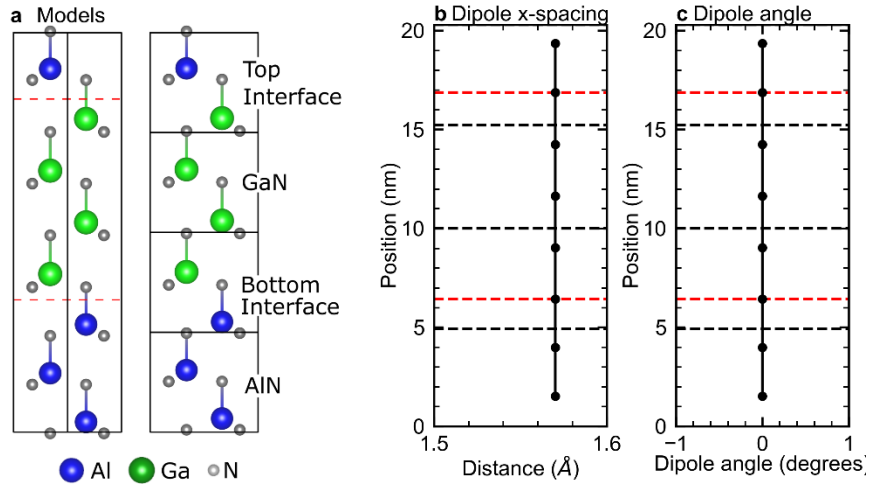

Figure S2. Extended structural information. (a) Model reproduced from **Figure 1**. (b) Spacing between the dipole centers along the x-direction (a-axis) showing a uniform dipole-dipole spacing in-plane. (c) Angle of the III-N dipole showing that all dipoles are aligned along the c-axis.

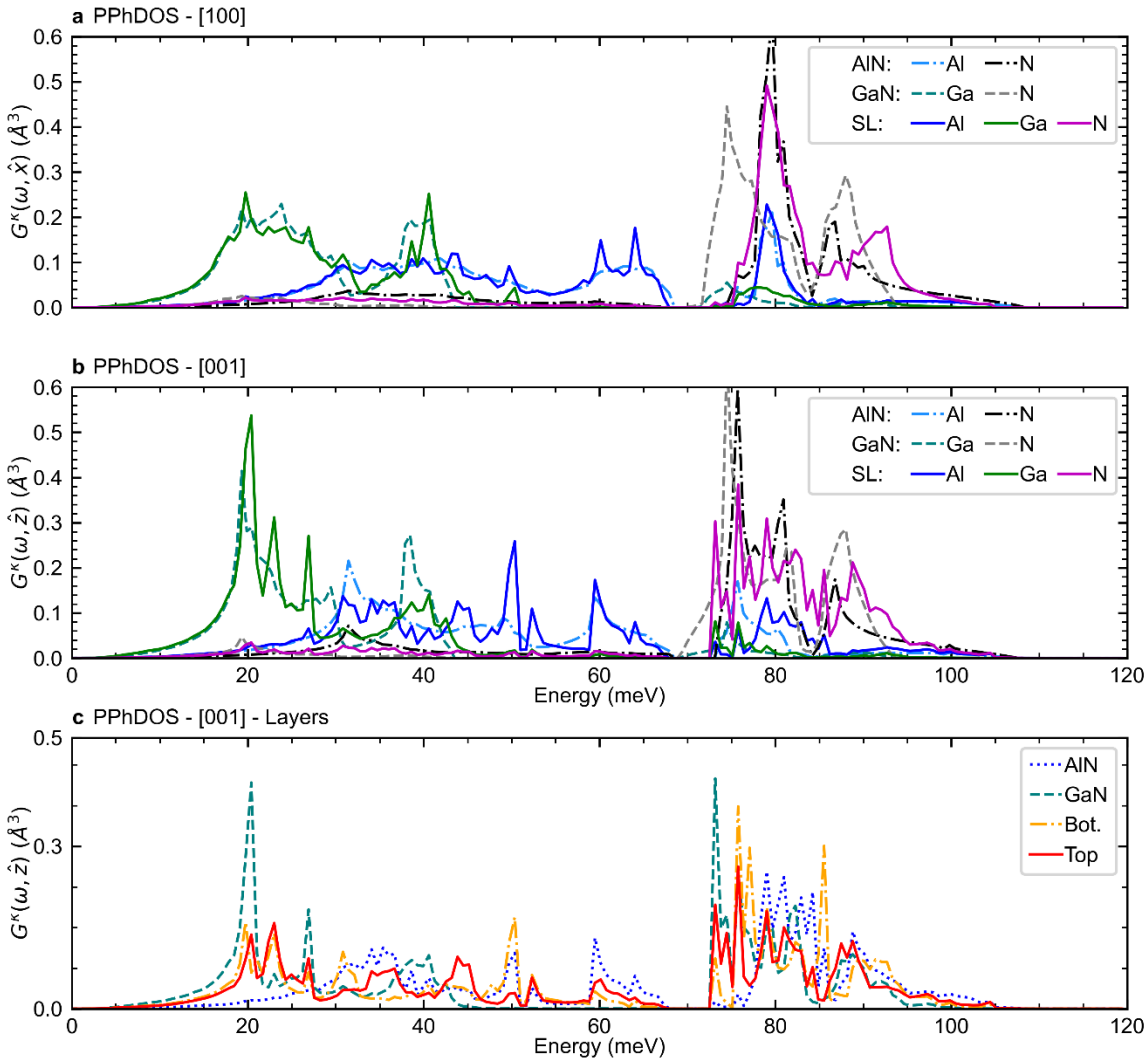

Figure S3. Element and layer PPhDOS. Element PPhDOS along the (a) $\boldsymbol{q}_x$ and (b) $\boldsymbol{q}_z$ axes. (c) Layer PPhDOS along the [001] axis.

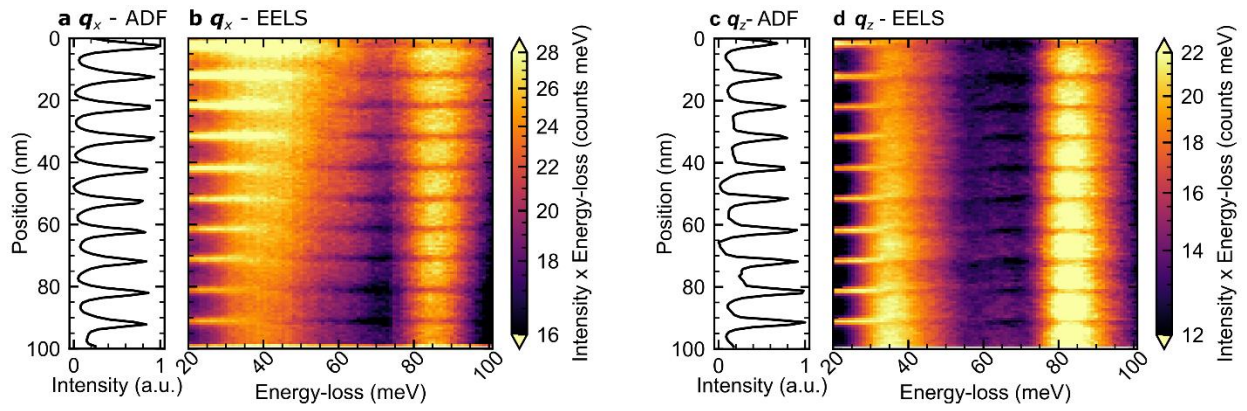

Figure S4. Full off-axis EELS line scans before projection. Line scan data before projection for the (a,b) $\boldsymbol{q}_x$ and (c,d) $\boldsymbol{q}_z$ off-axis conditions. (a,c) Show the ADF signal that has been background subtracted to remove thickness effect and improve period-to-period cross-correlation during projection. (c,d) Show the EELS line scans normalized by intensity to remove the elastic tail.

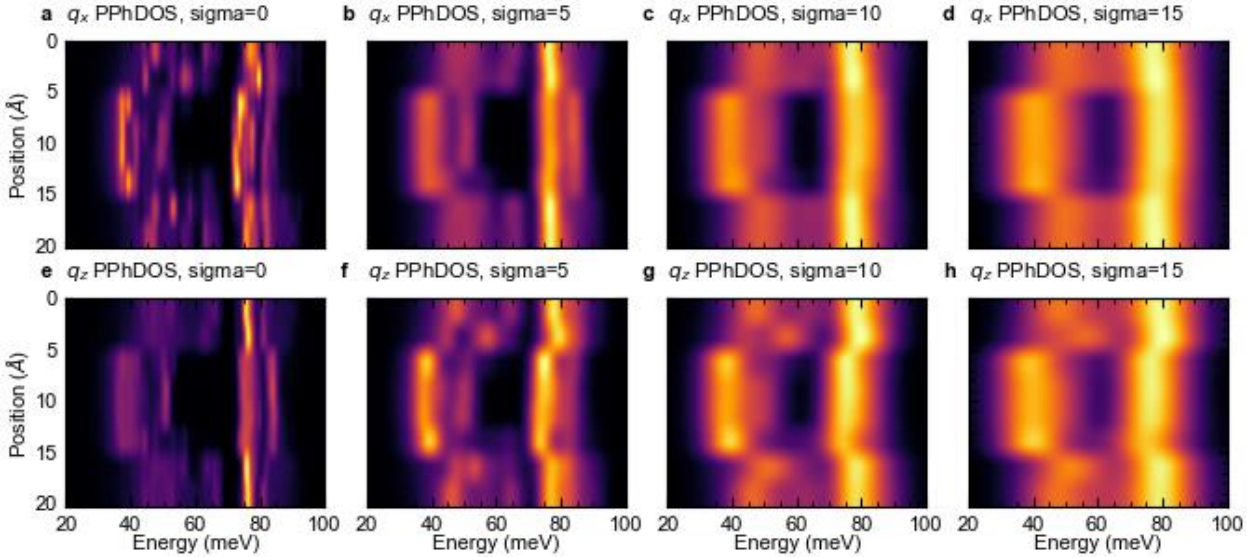

Figure S5. Heatmap of dipole PPhDOS across the SL with different blurring. Dipole PPhDOS along the (a-d) q_x and (e-h) q_z directions. Various degrees of Gaussian blur have been applied to simulate different instrument spectral resolution as indicated in the labels in units of meV.

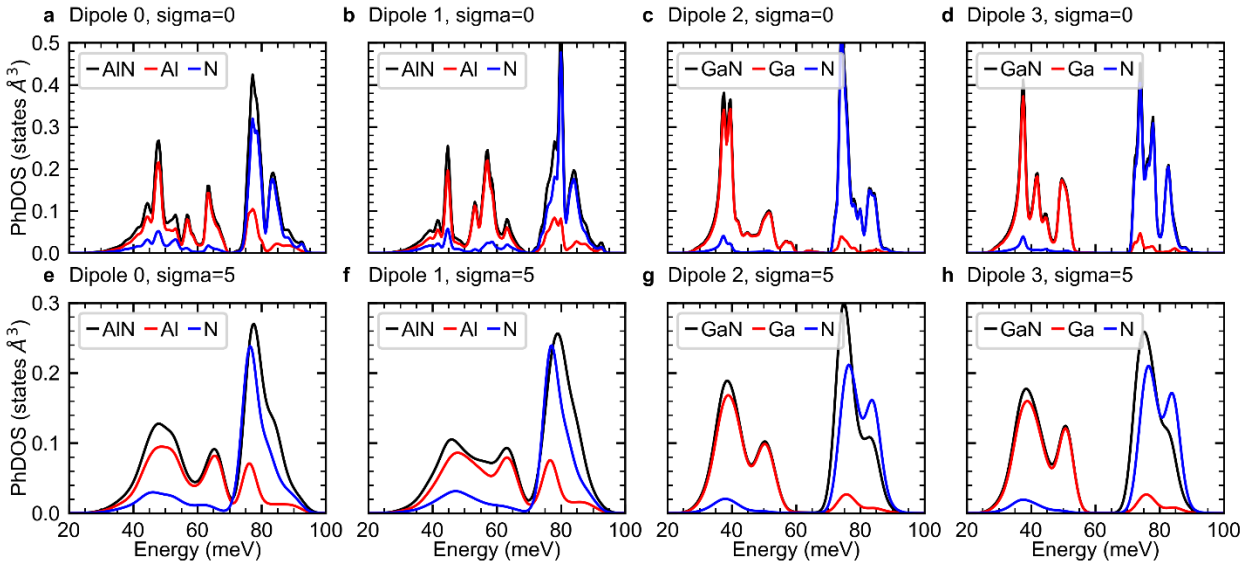

Figure S6. Dipole $10\bar{1}0$ PPhDOS across the top-interface. PPhDOS (a-d) with now blurring and (e-h) 5 meV of Gaussian blurring for the (a,e) AlN dipole in an AlN layer, (b,f) AlN dipole in the top-interface layer, (c,g) GaN dipole in the top-interface layer, and (d,h) GaN in the GaN layer.

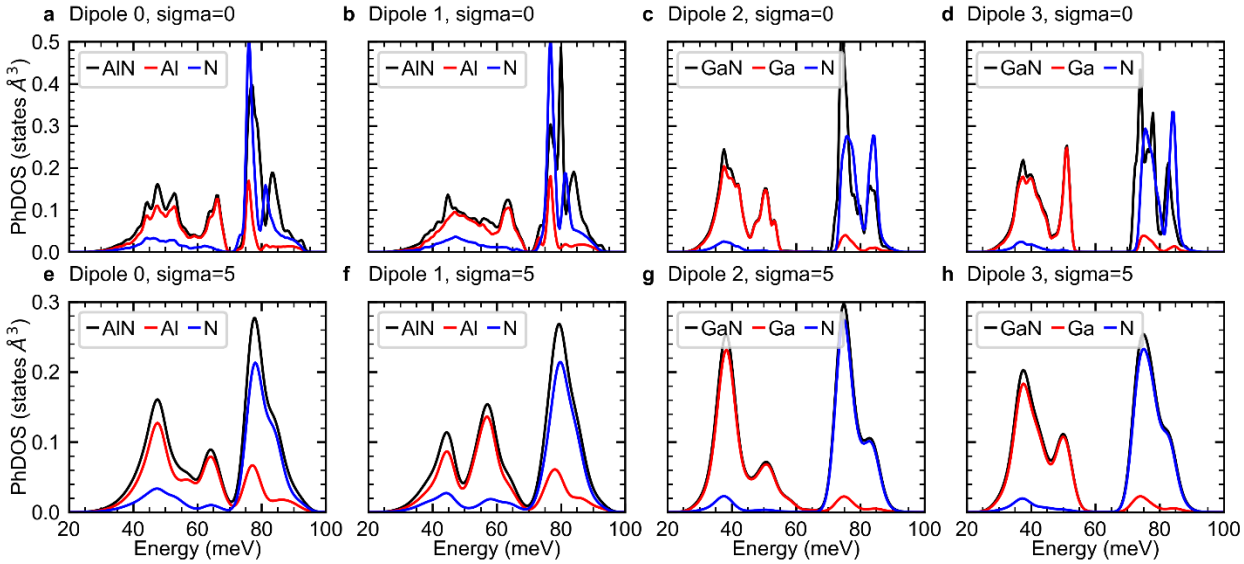

Figure S7. Dipole 0002 PPhDOS across the top-interface. PPhDOS (a-d) with now blurring and (e-h) 5 meV of Gaussian blurring for the (a,e) AlN dipole in an AlN layer, (b,f) AlN dipole in the top-interface layer, (c,g) GaN dipole in the top-interface layer, and (d,h) GaN in the GaN layer.

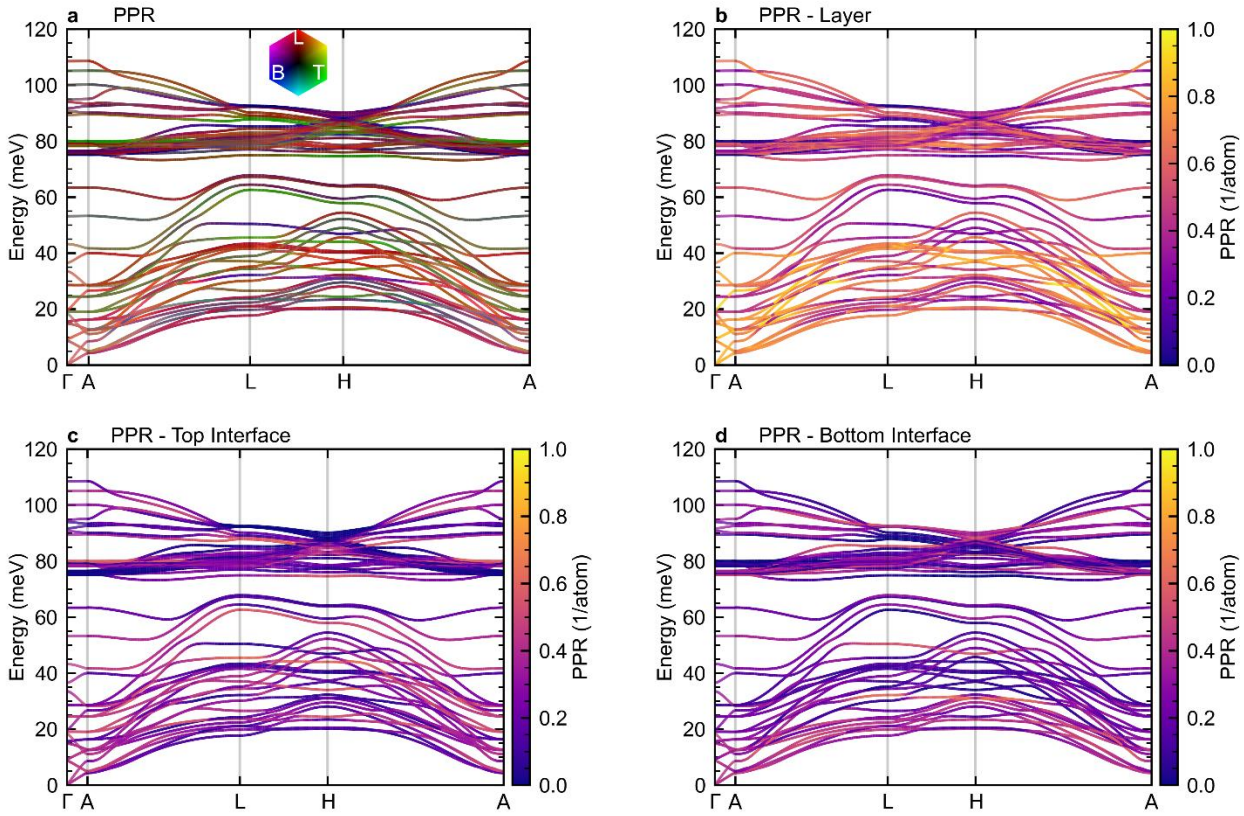

Figure S8. Quantitative layer PPR. (a) Layer PPR reproduced from **Figure 3**(b) showing qualitatively the relative contribution to PR from the three regions. More quantitative representation of PPR for the endmembers, namely the (b) layers, (c) top interface, and (d) bottom interface.

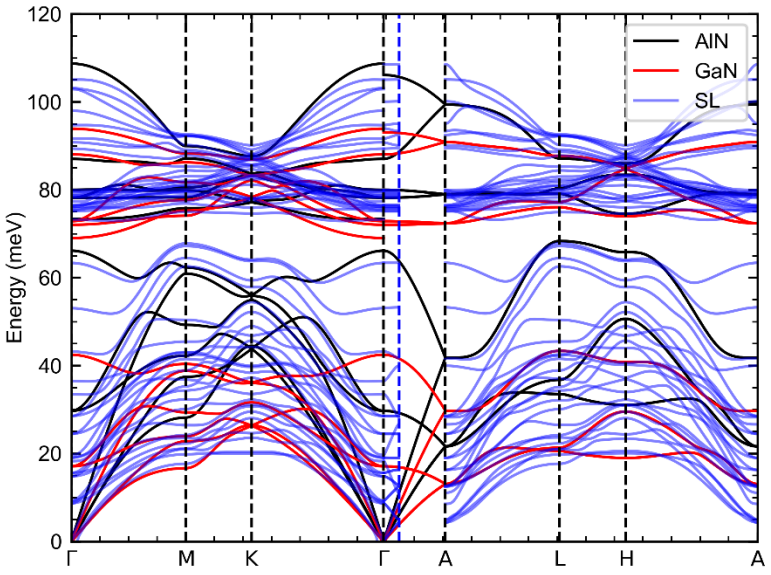

Figure S9. Phonon dispersion comparison between AlN, GaN, and SL. Phonon dispersions plotted together to show the relative energy and structures of bands. The Brillouin zones were all scaled to match, except for the SL Γ-A Brillouin zone that is ¼ of the AlN and GaN to match the Brillouin zone folding.

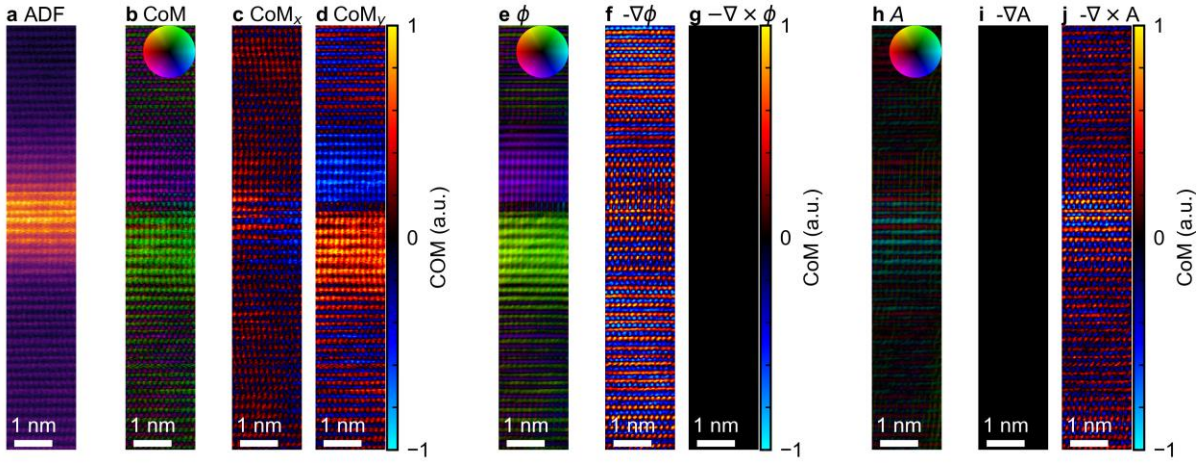

Figure S10. 4D-STEM CoM decomposition. (a) ADF signal reproduced from **Figure 1**(e). Raw CoM phase image calculated from the 4D-STEM dataset and its (c,d) cartesian components. (e) curl-free CoM reproduced from **Figure 1**(f). (f) Divergence and (g) curl of the curl-free CoM. (h) divergence-free CoM. (i) Divergence and (j) curl of the divergence-free CoM.

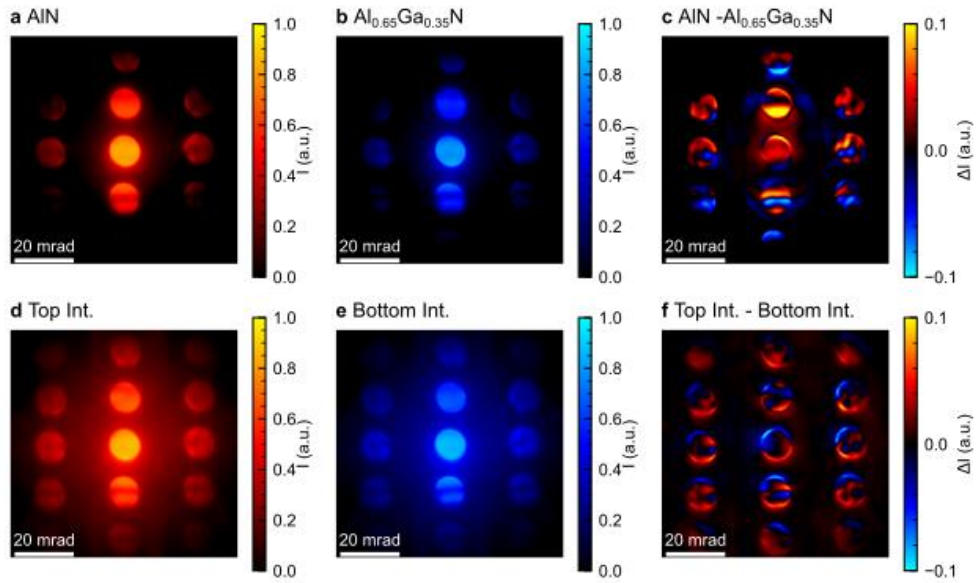

Figure S11. Qualitative symmetry differences in different layers from PACBED patterns. (a) AlN and (b) ($Al_{0.65}Ga_{0.35}$)N PACBED patterns. (c) Difference pattern between AlN and ($Al_{0.65}Ga_{0.35}$)N. PACBED patterns from the (d) top and (e) bottom-interfaces showing the broken Fresnel symmetry of the projected crystal structure. (f) Difference PACBED between the top and bottom-interface. Indexing is omitted for clarity, refer to **Figure 1**(g-i).

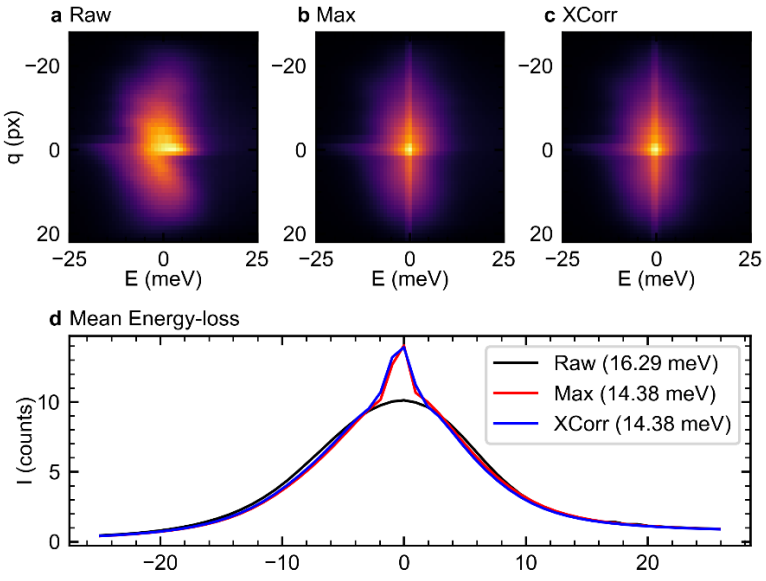

Figure S12. q_x off-axis quasi-elastic ZLP alignment method comparison. (a) Raw (b) maximum aligned, and (c) cross-correlated quasi-elastic ZLP. (d) Average quasi-elastic ZLP from each alignment method showing the best energy-resolution for cross-correlation. The three maximum values in the aligned spectra are ignored when measuring the FWHM to avoid biasing the resolution of the spurious low-signal alignments leading to the sharp peak.

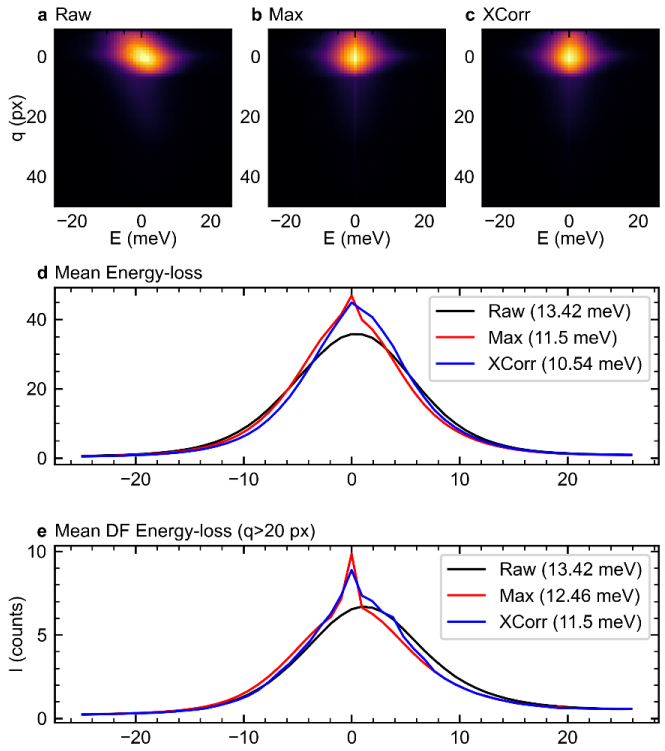

Figure S13. q_z off-axis quasi-elastic ZLP alignment method comparison. (a) Raw (b) maximum aligned, and (c) cross-correlated ZLP. (d) Average ZLP from each alignment method showing the best energy-resolution for cross-correlation. (e) Average correlated quasi-elastic ZLP from the darkfield signal showing the best energy-resolution for cross-correlation. The three maximum values in the aligned spectra are ignored when measuring the FWHM to avoid biasing the resolution of the spurious low-signal alignments leading to the sharp peak.

S2 Supplementary Information: 4D-STEM

We can qualitatively show the existence of different fields at the two interfaces that result from the structural differences using 4D-STEM CoM imaging (**Figure S10**(a-d)). We make note that CoM includes both electrostatic and diffraction effects (*e.g.*, channeling), and make no claims that the below results are purely from electrostatic effects. We already know that the fields exist in these and similar materials and differ to other studies for complex experiments that isolate different CoM contributions.[1–3]

Figure S10 shows the result of ADF and CoM vector images using 4D-STEM. For better interpretation of the result, we used Helmholtz decomposition to split the CoM vector field to a curl-free field (p_ϕ) and divergence-free field (p_A).[4] This procedure is done using Fourier analysis, as a vector field $\vec{p}(\vec{r})$ could be written as

$$\vec{p}(\vec{r}) = -\int\int\int i\,\vec{k}\cdot G_\phi(\vec{k})e^{i\vec{k}\cdot\vec{r}}dV_k + \int\int\int i\vec{k}\times\overrightarrow{G_A}(\vec{k})e^{i\vec{k}\cdot\vec{r}}dV_k = -\nabla\phi(\vec{r}) + \nabla\times\vec{A}(\vec{k})$$

where $p_\phi = -\nabla\phi(\vec{r})$ and $p_A = \nabla\times\vec{A}(\vec{k})$.

As shown in **Figure S10**(e-j), we show that Helmholtz decomposition successfully separate the curl-free and divergence-free component of the CoM image. As Zweck et al.[4] pointed out, a pure electrostatic field could only generate a curl-free phase shift to electron beam, therefore we interpret the curl-free field c_ϕ as the electrostatic field at the interface. Non-zero divergence-free field c_A is also observed (**Figure S10**(g-i)), which could have multiple origin, such as structural heterogeneity along the depth direction, dynamical scattering, miss tilt or slight misalignment in the diffraction pattern rotation and scan distortion. Further study is required to determine the origin of the non-zero c_A.

Apart from the observation of the electric field observed through CoM, we can look at the intensity distribution of PACBED patterns averaged from the two layers (**Figure S11**(a-c)) and two interfaces (**Figure S11**(d-f)). The distribution of intensity in the 0002 and $000\bar{2}$ are non-equivalent.

Figure S11(a,b) show the PACBED patterns from the layers of the SL. In both the $000\bar{2}$ has a dark line through the disc and the 0002 appear brighter, as expected from the Fresnel symmetry breaking in the Wurtzite crystal structure.[5,6] The difference pattern in **Figure S11**(c) does not show any immediately obvious intensity flux and the 0004 and $000\bar{4}$ reflections are symmetric about the center of the pattern, which suggests that difference in fluxes does not produce qualitative polarization fluxes when two different materials are compared. We attribute this feature to differences in angular scattering probability resulting from the different screened potentials of the two materials. For example, the AlN contains higher scattering probabilities peaked in the forward direction because of the lighter masses while $(Al_{0.65}Ga_{0.35})N$ scatters the electron to higher angles, leading to larger HAADF signal and less forward scattering. These differences lead to an unequal weighting for different scattering angles in different materials, which would overwhelm and non-faithfully represent intensity fluxes from lack of inversion symmetry.

On the other hand, PACBED patterns from materials containing approximately the same mass density would have similar scattering probability to different angles. This phenomenon can be seen in the PACBED patterns in **Figure 1**(g,h), reproduced in **Figure S11**(d,e), that are from the two interfaces. Both interfaces have approximately the same $Al_{0.825}Ga_{0.175}N$ composition but different atomic basis in the structural units. As a result, their scattering distributions comparable, and any intensity fluxes are a result of symmetry. However, the structural changes can still lead to channeling in addition to the polarization.

S3 Supplementary Information: DFT

Figure S1(b) shows the interatomic distance for atoms in the dipoles for each (0002) plane. The dipoles exhibit a similar trend to the pure III-V superlattice shown in **Figure 1**(c) except for large variability in the interatomic distance that results from the mixture of III-site elements in the alloy. One important feature in the alloy that is also like the pure AlN-GaN superlattice is the interatomic dipole distances at the bottom-interface having values smaller than the natural AlN layer.

Figure S2 shows additional information to **Figure 1**(c) and better informs about in-plane displacements and shear that could occur from putting to materials together in a heterostructure. No variability is observed in the in-plane spacing between dipoles and the angle of the dipole is zero across the full period. Both features indicates that no unique in-plane displacement structure exists across the structure and all the dipoles remain aligned with the *z*-axis.

The PPhDOS profiles in **Figure S5** and the dipole-PPhDOS in **Figure S6** and **Figure S7** include different levels of spectral blurring. From the comparison of the $\boldsymbol{q}_x$ to $\boldsymbol{q}_z$ in **Figure S5** it is clear that the Al vibrations exist in the $\boldsymbol{q}_x$ but are only resolvable with energy resolutions <5 meV. Additionally, the $\boldsymbol{q}_x$ does not show significant swooping relative to $\boldsymbol{q}_z$ for any level of blurring.

Figure S9 Shows the phonon dispersion for AlN, GaN, and the superlattice. The GaN dispersion and superlattice have been scaled to the Brillouin path distances of AlN so that the general characteristics of the dispersions can be compared. The energies and fractional path positions remain quantitatively accurate, while other derivative quantities (*e.g.*, group velocity, effective mass) are slightly distorted. The Γ-A path for the superlattice was corrected to be ¼ of the AlN Γ-A path to minimize the impact of the large *z*-axis difference between the AlN and GaN relative to the superlattice supercell. Such a scaling also emphasizes bands that have potentially folded from the endmember structures. The superlattice dispersion shows significant deviation from the

endmember dispersions that cannot be explained by band folding. Therefore, the phonons in the superlattice are strongly impacted by the interaction between the endmembers in this AlN-GaN material system. As discussed in the main text, a noticeable region of bands in the superlattice that are isolated from the endmembers fall in the GaN optical phonon gap from 43-69 meV.

S4 Comparison off-axis EELS to PPhDOS

The PhDOS is formally defined as $G(E) = \frac{1}{N}\sum_{\boldsymbol{q}j} \delta\left(\omega - \omega_{\boldsymbol{q}j}\right)$, where N is the number of atoms, δ is the Dirac-delta function, $\boldsymbol{q}j$ momentum at band index j, and ω frequency. The PhDOS can be atom- and direction-projected to the PPhDOS with $G_\kappa(\omega, \hat{\boldsymbol{q}}_n) = \frac{1}{N}\sum_{\boldsymbol{q}j} \left|\hat{\boldsymbol{q}}_n \cdot \mathbf{e}_\kappa^j\right|^2 \delta\left(\omega - \omega_{\boldsymbol{q}j}\right)$, where $\hat{\boldsymbol{q}}_n$ is the projected unit vector, **e** the eigenvector displacements, and κ is the atom index. As we noted in the main text, this definition parallels the direction-projection used in the EELS scattering cross-section[7,8] defined by

$$\frac{\mathrm{d}^2\sigma}{\mathrm{d}\Omega \mathrm{d}\omega}(\boldsymbol{q}, \omega) = \frac{4\hbar}{a_0^2 |\boldsymbol{q}|^2} \sum_j \frac{1 + f_{\boldsymbol{q}j}}{\omega_{\boldsymbol{q}j}} \left| \sum_\kappa \frac{1}{\sqrt{M_\kappa}} Z_\kappa(\boldsymbol{q}) \cdot \mathbf{e}_\kappa^j e^{-i\boldsymbol{q}\cdot r_\kappa} \right|^2 \delta\left(\omega - \omega_{\boldsymbol{q}j}\right)$$

where $\hbar$ is the reduced Plank's constant, a_0 the Bohr radius, $f_{\boldsymbol{q}j}$ is the non-equilibrium phonon population, M is the atomic mass, r_κ are atomic positions, and $Z_\kappa(\boldsymbol{q}) = -i\frac{V}{|\boldsymbol{q}|}\Delta n_\kappa(\boldsymbol{q}) e^{-i\boldsymbol{q}\cdot r_\kappa} + \frac{\boldsymbol{q}}{|\boldsymbol{q}|} Z_\kappa^{\mathrm{ion}}$ is the Fourier-transform of the effective charge that accounts for both the ion and valence-electron-density response (n_κ) from the moving ion. In the large $\boldsymbol{q}$ limit of off-axis EELS, $Z_\kappa(\boldsymbol{q}) = \frac{\boldsymbol{q}}{|\boldsymbol{q}|} Z_\kappa^{\mathrm{ion}}$, and therefore,

$$\frac{\mathrm{d}^2\sigma_{\mathrm{off}}}{\mathrm{d}\Omega \mathrm{d}\omega}(\boldsymbol{q}, \omega) \propto \sum_{j,\kappa} \left| \frac{\boldsymbol{q}}{|\boldsymbol{q}|} \cdot \mathbf{e}_\kappa^j \right|^2 \delta\left(\omega - \omega_{\boldsymbol{q}j}\right)$$

With the entrance aperture of the spectrometer acting as a filter, we choose a select portion of scattering space, which is equivalent to the $\hat{\boldsymbol{q}}_n$ used in the direction PPhDOS. We, therefore, have agreement between the direction PPhDOS and the scattering cross-section both containing a

$$\left|\hat{\boldsymbol{q}}_n \cdot \mathbf{e}_\kappa^j\right|^2 \delta\left(\omega - \omega_{\boldsymbol{q}j}\right)$$

.

S5 Supplementary Information: References

1. Toyama, S. *et al.* Quantitative electric field mapping in semiconductor heterostructures via tilt-scan averaged DPC STEM. *Ultramicroscopy* **238**, 113538 (2022).
2. Toyama, S. *et al.* Real-space observation of a two-dimensional electron gas at semiconductor heterointerfaces. *Nat. Nanotechnol.* **18**, 521–528 (2023).
3. Müller-Caspary, K. *et al.* Electrical Polarization in AlN/GaN Nanodisks Measured by Momentum-Resolved 4D Scanning Transmission Electron Microscopy. *Phys. Rev. Lett.* **122**, 106102 (2019).
4. Zweck, J., Schwarzhuber, F., Pöllath, S. & Müller-Caspary, K. Advanced processing of differential phase contrast data: Distinction between different causes of electron phase shifts. *Ultramicroscopy* **250**, 113752 (2023).
5. Imura, M. *et al.* Analysis of Broken Symmetry in Convergent-Beam Electron Diffraction along and Zone-Axes of AlN for Polarity Determination. *Jpn. J. Appl. Phys.* **52**, 08JE15 (2013).
6. Berger, A. Inversion Domains in Aluminum Nitride. *J. Am. Ceram. Soc.* **74**, 1148–1151 (1991).
7. Senga, R. *et al.* Imaging of isotope diffusion using atomic-scale vibrational spectroscopy. *Nature* **603**, 68–72 (2022).
8. Gadre, C. A. *et al.* Nanoscale imaging of phonon dynamics by electron microscopy. *Nature* **606**, 292–297 (2022).